Published December 13, 2016

Robust gap repair in the contractile ring ensures timely completion of cytokinesis

Ana M. Silva,[1,2] Daniel S. Osório,[1,2] Antonio J. Pereira,[1,2] Helder Maiato,[1,2] Inês Mendes Pinto,[3] Boris Rubinstein,[4] Reto Gassmann,[1,2] Ivo Andreas Telley,[5] and Ana Xavier Carvalho[1,2]

[1]Instituto de Investigação e Inovação em Saúde, Universidade do Porto, 4200-135 Porto, Portugal
[2]Instituto de Biologia Molecular e Celular, 4200-135 Porto, Portugal
[3]International Iberian Nanotechnology Laboratory, 4715-330 Braga, Portugal
[4]Stowers Institute for Medical Research, Kansas City, MO 64110
[5]Instituto Gulbenkian de Ciência, Fundação Calouste Gulbenkian, 2780-156 Oeiras, Portugal

Cytokinesis in animal cells requires the constriction of an actomyosin contractile ring, whose architecture and mechanism remain poorly understood. We use laser microsurgery to explore the biophysical properties of constricting rings in *Caenorhabditis elegans* embryos. Laser cutting causes rings to snap open. However, instead of disintegrating, ring topology recovers and constriction proceeds. In response to severing, a finite gap forms and is repaired by recruitment of new material in an actin polymerization–dependent manner. An open ring is able to constrict, and rings repair from successive cuts. After gap repair, an increase in constriction velocity allows cytokinesis to complete at the same time as controls. Our analysis demonstrates that tension in the ring increases while net cortical tension at the site of ingression decreases throughout constriction and suggests that cytokinesis is accomplished by contractile modules that assemble and contract autonomously, enabling local repair of the actomyosin network. Consequently, cytokinesis is a highly robust process impervious to discontinuities in contractile ring structure.

Introduction

Cytokinesis, the process that completes cell division by partitioning the contents of the mother cell to the two daughter cells, requires the assembly and constriction of a contractile ring (Green et al., 2012). The contractile ring is composed of a network of actin filaments and nonmuscle myosin II motor proteins, whose architecture and mechanism of constriction remain poorly understood. The contractile ring could be composed of a series of contractile units (Bement and Capco, 1991; Savoian et al., 1999; Carvalho et al., 2009), although a modular organization has so far not been observed by EM (Kamasaki et al., 2007). Alternatively, the ring could be a dynamic actomyosin bundle based on work in fission yeast protoplasts, as proposed by Stachowiak et al. (2014). Laser microsurgery has provided powerful insight into cellular actomyosin structures and has been used to study wound healing (Mandato and Bement, 2001), stress fibers (Kumar et al., 2006; Colombelli et al., 2009), cortex dynamics (Tinevez et al., 2009), cohesion of the epithelial tissue during cell division (Founounou et al., 2013; Guillot and Lecuit, 2013; Herszterg et al., 2013), and shape changes during tissue morphogenesis (Collinet et al., 2015; Munjal et al., 2015). In this study, we combine laser microsurgery with live imaging in the *Caenorhabditis elegans* early embryo to probe the biophysical properties of constricting contractile rings during cytokinesis.

Correspondence to Ana Xavier Carvalho: anacarvalho@ibmc.up.pt

Abbreviations used: CI, confidence interval; PH, pleckstrin homology.

Results and discussion

In the four-cell embryo, two cells (ABa and ABp) undergo contractile ring constriction parallel to the focal plane, which provides an end-on view of the constricting ring when made visible under the microscope and facilitates the monitoring of shape change and ring component dynamics (Fig. S1 A). Furthermore, these cells are relatively large, with a contractile ring perimeter of 55.8 ± 0.4 µm (mean ± 95% confidence interval [CI]) at constriction onset, and divide with highly reproducible kinetics, enabling spatiotemporal measurements and analysis (Fig. S1, D and E). The velocity of ring constriction is roughly constant until the ring approaches the spindle midzone, when ring closure slows down until constriction completes (Fig. S1 E; Carvalho et al., 2009).

Using nanosecond laser pulses, we severed rings of ABa and ABp cells expressing myosin$^{NMY\text{-}2}$::GFP, a fluorescent nonmuscle myosin II heavy chain that localizes in the ring and in the remaining cell cortex at different stages of constriction, without damaging the adjacent plasma membrane (Fig. S1, A and B; Fig. S2, A–C; and Video 1). Contractile rings exhibited a fast mechanical change of length and curvature, snapping

Supplemental Material can be found at:
/content/suppl/2016/12/12/jcb.201605080.DC1.html

The Rockefeller University Press $30.00
J. Cell Biol. Vol. 215 No. 6 789–799
https://doi.org/10.1083/jcb.201605080

Published December 13, 2016

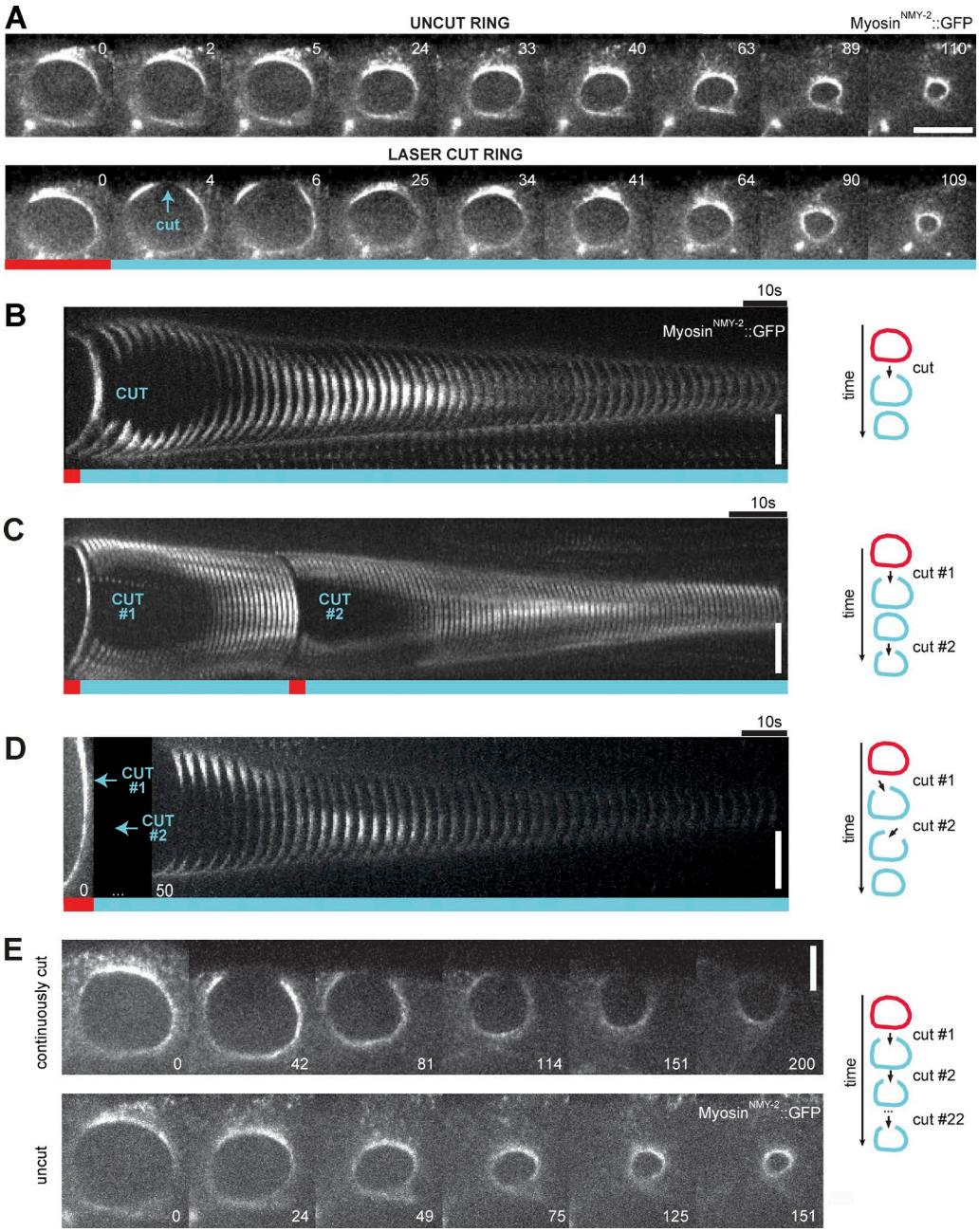

Figure 1. **Behavior of contractile rings severed by laser microsurgery during constriction.** (A) End-on view stills from time-lapse imaging series of constricting contractile rings in ABp cells expressing myosin^{NMY-2}::GFP. The contractile ring snaps open after the laser cut (cyan arrow, frame 4), the gap is repaired (frame 25), and ring constriction resumes to completion. (B–D) Kymographs of ring regions cut by laser microsurgery built as depicted in Fig. S1 E. The time interval between frames is 2.32 s in B, 1 s in C, and 3.2 s in D. Rings were subjected to a single cut (B), or to two sequential cuts with the second cut either hitting the same region (C) or a neighboring region (D). Time-lapse acquisition in D resumed after both cuts were executed (missing frames are indicated by a black box). (E) Stills of a constricting ring with a persistent gap, which was maintained by iteratively cutting the same site. Time is in seconds, and time zero denotes the frame before the laser cut. Bars, 5 µm.

open immediately after the cut. Surprisingly, rings neither regressed completely nor showed signs of disintegration. Instead, after finite retraction of the severed ends, the gap was repaired (Fig. 1, A and B; and Video 1). These results are similar to those obtained in laser-cutting experiments for actomyosin rings bordering plasma membrane wounds in *Xenopus* oocytes (Mandato and Bement, 2001). In our experiments, the gap was rapidly filled in with myosin^{NMY-2}::GFP and ring constriction resumed. Severed rings always successfully completed constriction (n = 75), and embryos continued to develop (7 out of 11 tracked embryos hatched, and the remaining embryos arrested during elongation, a late stage of embryogenesis). A striking finding is that despite locally destroyed ring topology, the resulting ring fragment retained most of its shape, which implies that it is anchored to the plasma membrane. Moreover, a mechanism is in place to repair gaps in the contractile ring at any stage of constriction, invariably allowing for the successful conclusion of cytokinesis.

To assess the robustness of contractile ring repair, we performed sequential cuts on the same constricting ring. In one set of experiments (n = 6; Fig. 1 C), the second cut was made at the

Published December 13, 2016

site of the first cut after the gap had been repaired (Video 2). In another set of experiments, sequential cuts were made in spatially separate regions 20–25 s apart (n = 8; Fig. 1 D). Similar to rings that were cut once, rings cut twice with either cutting regimen repaired the gaps and completed constriction. These results demonstrate that ring gap repair is history independent and is a locally autonomous process that is not influenced by events in adjacent regions of the ring.

To test whether gaps in contractile ring structure must be repaired in order for constriction to proceed, we made 22 consecutive cuts on the same side of a constricting ring, thus preventing it from resealing for 300 s. Strikingly, the ring fragment shortened from 30 µm to 10 µm during this time (Fig. 1 E and Video 3). Although the ring fragment constricted at a reduced velocity compared with uncut control rings, this experiment shows that a continuous contractile ring structure is not a prerequisite for constriction and is in agreement with the early observations that isolated fragments of cleavage furrows from dividing newt eggs are able to constrict in a buffer containing ATP (Mabuchi et al., 1988).

Next, we followed the initial response of severed rings with high temporal resolution. Immediately after the laser cut, ring snapping implied that the ring was under tension. Moreover, the severed ends no longer followed the curvature of the ring, instead adopting a straight conformation (71 out of 75 cut rings; Fig. 2 A), implying that the ring is working against cortical or membrane tension, as ring constriction is influenced by the mechanical properties of the remaining cell cortex (Zhang and Robinson, 2005; Turlier et al., 2014; Sain et al., 2015). We consistently observed this change in curvature in rings marked with other contractile ring components, including lifeAct::GFP (marking actin) and GFP::septin^{UNC-59} (Fig. S2 E). Moreover, we observed a corresponding deformation of the plasma membrane at the cut site using GFP::PH$^{PLC1\delta1}$ as a marker (Fig. S2 F), which revealed local relaxation of the plasma membrane at the tip of the septum. The curvature of the plasma membrane recovered 10–15 s after the cut (Fig. S2 F).

We were able to accurately follow the severed ends of cut rings, which allowed us to determine the gap size and the length of the cut ring (arc length) for 10 s after the cut (Fig. 2). The response to the laser cut resembled a viscoelastic mechanical relaxation, similar to what has been described for rings in an epithelial tissue (Guillot and Lecuit, 2013). At least two phases of gap formation after microsurgery were detectable within our temporal resolution: a fast phase of elastic recoil and a slow ("creep") phase that lasted for ∼6 s after the cut. Then the gap size remained roughly constant for ∼4 s and subsequently decreased in a phase of repair (Figs. 2 C and S2 D). Plotting gap size at a time when the gap had widened to its maximum (∼6 s after laser cutting; Fig. 2 C) and reached 20.2 ± 0.9% of the initial perimeter (Fig. S2 D) revealed a proportional increase between gap size and initial ring perimeter (Fig. 2 D).

To gain mechanical insight, we estimated ring recoil and cortical relaxation for cut rings with different initial perimeters (see Materials and methods for details). Ring recoil after laser cutting (Δl) is the change in arc length caused by tension and equals the initial ring perimeter minus the ablated length minus the arc length. The ablated length corresponds to the ring material removed by the laser spot, which is ∼0.5 µm, and the arc length was measured 3.6 or 3.9 s after laser cutting (see Materials and methods for details). We found that Δl decreases as the perimeter decreases (Fig. 2 E, blue, orange, and green circles). The strain of the ring (ε), which corresponds to the tension in the intact ring according to Hooke's law, is defined as Δl divided by the arc length (in the absence of tension). We found an increase in ring tension with decreasing perimeter (Fig. 2 F, blue, orange, and green circles). In contrast to the prediction of a static theoretical model whereby tension in the ring decreases proportionally to ring perimeter (Sain et al., 2015), our result reflects the dynamic and static force components that the constricting ring has to work against. One of the dynamic components could be the viscous drag forces caused by septum area growth that are expected to increase with constriction (Fig. S1 B). An increase in the strain of the ring at the last stages of constriction would be in agreement with the increase in the concentration of contractile ring components that is observed for smaller perimeters (Carvalho et al., 2009).

Gap size is the consequence of (a) ablated material, (b) ring recoil, and (c) stress relaxation in the cortex or membrane of the two forming cells behind the contractile ring, which changes ring curvature. Therefore, cortical relaxation corresponds to gap size minus Δl, and we found that it decreases proportionally to the decrease in ring perimeter (Fig. 2 G, blue, orange, and green circles; n = 22; R^2 = 0.84). We found that for large perimeters, the gap size is mostly determined by cortex relaxation (∼5 µm for a perimeter of 40 µm; Fig. 2 G) rather than ring recoil (∼2 µm, 5% of 40 µm; Fig. 2 E). For smaller perimeters, the contributions of cortex relaxation and ring recoil are roughly equal (∼1 µm).

The prediction of this mechanical dissection is that, in an embryo with reduced or no cortical tension, the difference between gap size and ring recoil should vanish, but the tension in the ring should still be nonzero and should increase during constriction. To test this prediction, we calculated ring strain (ε) and the gap size minus Δl in laser ablation experiments with embryos partially depleted of mlc-4, the regulatory light chain of nonmuscle myosin II. The regulatory light chain of nonmuscle myosin II is essential for myosin filament assembly and actomyosin contractility, which in turn determines cortical tension (Tinevez et al., 2009; Vicente-Manzanares et al., 2009). As expected, embryos partially depleted of mlc-4 exhibited a significant drop of cortical tension throughout constriction (Fig. 2 G, gray circles), and severed ends did not straighten (i.e., the curvature of the open ring did not change when compared with that of the intact ring; Fig. 2 H). Notably, in agreement with our prediction, the strain in the ring still increased during constriction (Fig. 2 F, gray circles). Collectively, our mechanical dissection suggests that at the onset of ring constriction, the tension born by the ring is predominantly determined by balancing cortical tension. In the course of constriction, when the perimeter decreases and the septum area increases, cortex and membrane tension are still present but decreasingly resist ring constriction. Instead, the ring works increasingly against dynamic force components, such as viscous friction and surface production. The net sum of static (Sain et al., 2015) and dynamic force components increases for decreasing perimeters along with time before it drops to zero at the end of constriction (Fig. 2 I).

After the immediate elastic recoil of the cut ring, the arc length of the initially larger rings continued to decrease while that of smaller rings did not show a clear tendency to further constrict until complete repair (Fig. 2 J). Nevertheless, this, together with evidence from the repeated ablation experiment (Fig. 1 E), indicates that the presence of the gap did not impact the ability of the open ring to constrict. It also suggests that

Published December 13, 2016

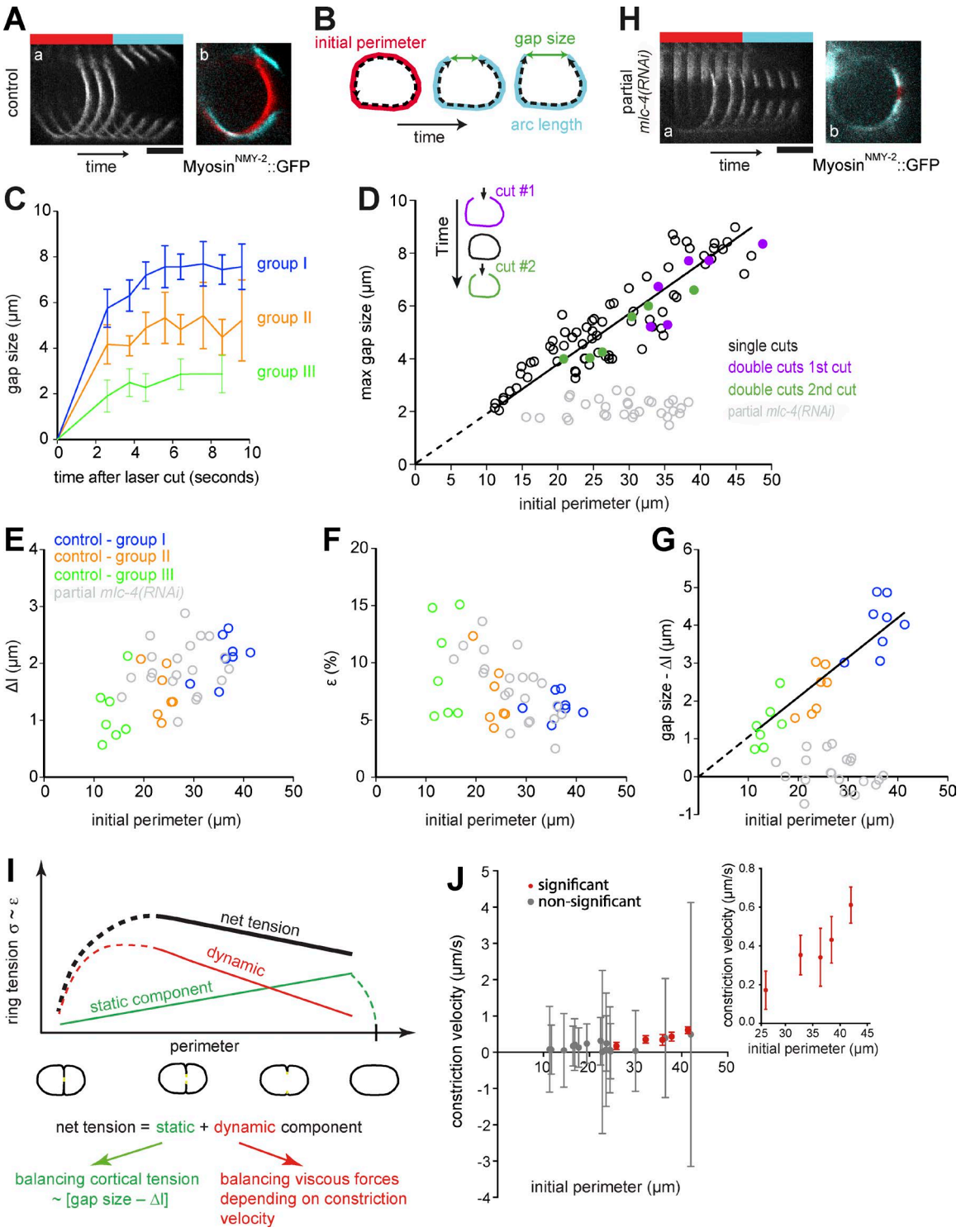

Figure 2. **Mechanical dissection of ring tension and cortical relaxation throughout ring constriction.** (A) Kymograph of the cut ring region showing the snapping event and straightening of the severed ends (a). The time interval between frames 3 and 4 is 2.6 s; other frames are 1 s apart. The overlay (b) shows frames immediately before (red) and after (cyan) the cut. (B) Schematic defining initial ring perimeter before the cut, arc length, and gap size. (C) Gap size measured during the first 10 s after the cut ($n = 24$). Cut rings were divided into three groups with initial perimeter averages of 35.8 µm (group I), 23.6 µm (group II), and 14.6 µm (group III). (D) Maximal gap size plotted against the initial perimeter for control rings cut once (black circles, $n = 69$) or twice, as in Fig. 1 C (first cut in purple, second cut in green; $n = 6$). Maximum gap size and initial perimeter are proportional ($R^2 = 0.81$ and $r = 0.90$; $P < 0.0001$). Maximum gap size for rings of mlc-4–depleted embryos are in gray. (E–G) Ring recoil (ΔI; E), strain of the ring (ε; F), and the difference between gap size and ΔI reflecting ring curvature change (G) plotted against the initial perimeter for control (blue, orange, and green circles, color coded as in C; $n = 22$) or mlc-4–depleted rings (gray circles; $n = 20$). In G, a clear proportionality is observed ($R^2 = 0.84$ and $r = 0.92$; $P < 0.0001$). (H) As in A, but for a cut ring of an embryo partially depleted of mlc-4. The time interval between frames 3 and 4 is 3.92 s; other frames are 2.32 s apart. (I) Schematic illustrating how the net tension results from the sum of static and dynamic components and increases for decreasing perimeters. (J) Rate of change in arc length during the first 8 s after cut against the initial perimeter (left). Significant values are in red and nonsignificant in gray. Error bars represent the 95% CI. An inset of the red points is shown (right). Bars, 5 µm.

Published December 13, 2016

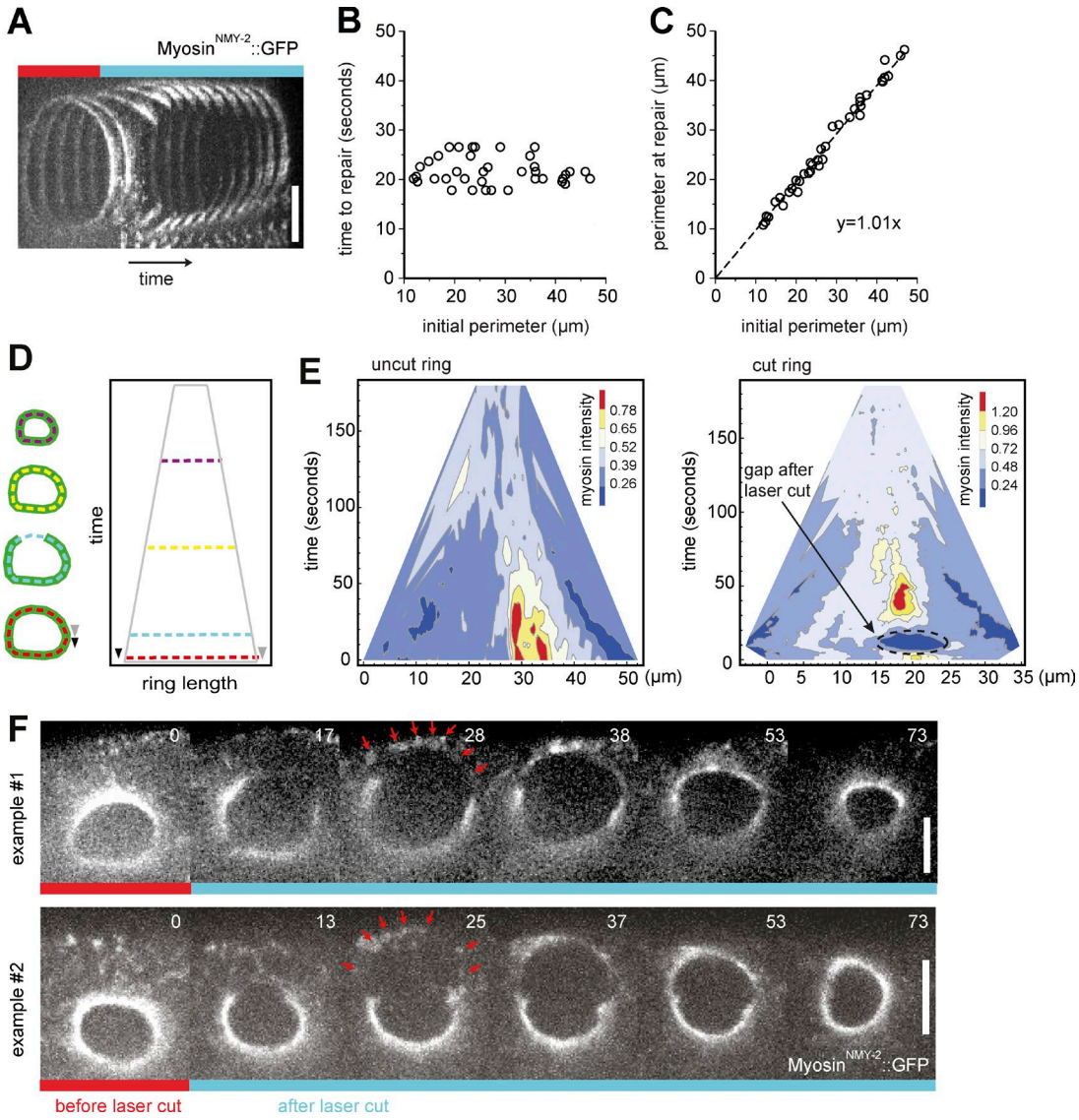

Figure 3. **Analysis of repair after laser microsurgery in contractile rings.** (A) Kymograph of the cut ring region showing that ring curvature is recovered by the end of gap repair. (B) Time between the laser cut and completion of gap repair plotted against the initial perimeter (n = 38). (C) The perimeter at the time of completion of repair plotted against the initial perimeter, showing a strong correlation (n = 38; R^2 = 0.99 and r = 0.99; P < 0.0001). (D) Schematic illustrating how heat maps of myosin^{NMY-2}::GFP distribution along the contractile ring circumference over time shown in E were generated. (E) Heat maps for myosin^{NMY-2}::GFP as described in D. (F) Stills of two cut rings that fail the first repair attempt. Red arrows point to foci of myosin^{NMY-2}::GFP that accumulate de novo along the length of the gap. Time is in seconds, and time zero corresponds to the frame before the laser cut. Bars, 5 μm.

either some other mechanical component, such as the cell cortex or the plasma membrane, assists ring constriction or that the remaining ring arc is still able to do work.

After gap widening (i.e., 6 s after the cut), a 12-s period followed when we could not accurately identify the severed ends. During this time, gaps were completely filled in with myosin^{NMY-2}::GFP, lifeAct::GFP, and GFP::septin^{UNC-59} (Fig. 1, A and B; and Fig. S2 E) so that 21.9 ± 1.0 s after the laser cut, all gaps were undetectable and a closed ring topology was reestablished (Fig. 3, A and B). We considered this to be the time point when gap repair was complete. Therefore, the time required for cut rings to completely repair gaps ranging from 2.1 to 8.9 μm was constant. Interestingly, the perimeter at which repair completed matched the initial perimeter (Fig. 3 C), indicating that the previous ring tension was established. In agreement with this, in cases where constricting rings were cut sequentially (Fig. 1 C), maximum gap size after the second cut was proportional to the initial perimeter before the second cut. This demonstrates that the tensions at the time of gap repair had been reestablished (Fig. 2 D, green and purple circles).

The invariable time to complete ring repair suggests that contractile ring components were recruited along their entire length of the gap, as gap closure from severed ends would be predicted to take longer for larger gaps. In agreement with this, myosin intensity profiles along the circumference of the ring revealed no significant lateral mobility from within the ring toward the gap (Fig. 3, D and E). Analysis of a minority of cut rings (2 out of 71), in which the first attempt at gap repair failed and the plasma membrane regressed more than usual, lent further support to this idea. In these two cases, myosin recruitment could be observed throughout the membrane at distinct foci (Fig. 3 F, arrows; and Video 4), and the gap was completely filled in with

Published December 13, 2016

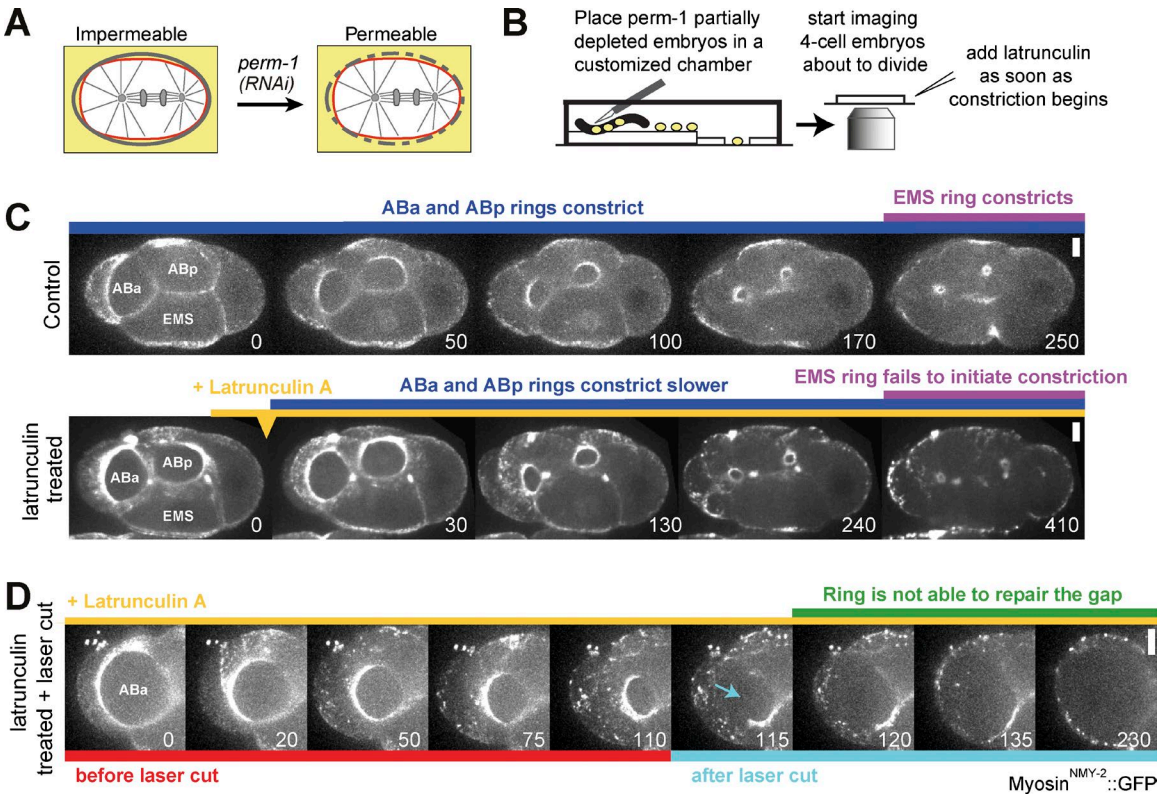

Figure 4. **Treatment with low doses of latrunculin A prevents ring repair after laser microsurgery.** (A and B) Schematics illustrating the procedure for embryo permeabilization (A) and live imaging combined with acute drug treatment (B). (C) Stills of control and latrunculin A–treated permeable embryos. (D) Stills of a latrunculin A–treated ABa cell, whose constricting ring was laser cut at the indicated time (cyan arrow). Time is in seconds. Bars, 5 µm.

myosin$^{NMY\text{-}2}$::GFP 20 s after the first failed repair (35 s after the cut). We conclude that within ∼22 s of being severed by laser microsurgery, constricting contractile rings have repaired their gaps from multiple sites along the exposed plasma membrane.

The multiple sites of myosin recruitment along the gap are likely to correspond to foci where new actin filament nucleation occurs. To test whether actin polymerization is required for gap repair, we treated permeabilized four-cell embryos with low doses of latrunculin A, which prevents new actin polymerization by sequestering actin monomers (Fig. 4, A and B). If added before furrow ingression, latrunculin A inhibits ring constriction altogether (Fig. 4 C, EMS cell). When added after ring constriction initiates, latrunculin A allows control rings to keep constricting (albeit slower than untreated rings; Fig. 4 C) but completely prevents ring resealing after laser microsurgery (Fig. 4 D). This shows that actin filament polymerization is essential for ring repair.

To examine the impact of the repair process on the kinetics of ring constriction, we analyzed the rate of change in ring perimeter after repair. Remarkably, this analysis revealed that cut rings took the same time to constrict to completion as uncut control rings (Fig. 5 A and Video 1). Inspection of individual traces revealed that the constriction velocity of cut rings was on average 35% higher than that of uncut control rings ($n = 15$; Fig. 5 B). Cut rings eventually caught up with uncut control rings likely because of their proximity to the spindle midzone. The spindle midzone has been shown to slow down contractile ring constriction (Carvalho et al., 2009), suggesting that it imposes a limit on the interval during which repaired rings can close with an increased constriction velocity. In agreement with this, repaired rings with larger initial perimeters, which started further away from the spindle midzone, closed with an increased constriction velocity for a longer time before their perimeters caught up with the mean perimeter of uncut control rings ($R^2 = 0.59$; Fig. 5 C). Along with accelerated constriction, we observed transient myosin accumulation in the repaired region greater than the mean myosin levels in that region before the cut. Myosin levels peaked 45.2 ± 1.9 s after the cut and then decreased and stabilized at ∼0.6 times the initial value, 73.9 ± 4.7 s after the cut (Figs. 5 D and S3, B and F). Actin also accumulated in the same region, with levels peaking 26.2 ± 1.5 s after the cut (Figs. S2 E and S3 B). Interestingly, the increase in myosin levels beyond the stabilization level roughly coincided with the time of repair completion, always occurring within the interval of increased constriction velocity (Fig. 5, B and D; and Fig. S3 F). We conclude that, after complete gap repair and recovery of ring topology, cut rings transiently recruit an excess of myosin to the repair site and speed up constriction, allowing them to complete cytokinesis in the same time as uncut rings.

Our analysis of contractile ring dynamics after laser microsurgery provides strong support for the previously proposed model that constriction is powered by a series of contractile units of equal size that locally constrict the plasma membrane at a constant velocity and make additive contributions to the overall constriction velocity (Carvalho et al., 2009). We propose that contractile units are connected to one another such that the contractile ring is able to sustain tension. The functional autonomy of individual contractile units explains the observation that constriction proceeds despite the presence of a gap in the ring circumference. Furthermore, units must be anchored to the membrane and/

Published December 13, 2016

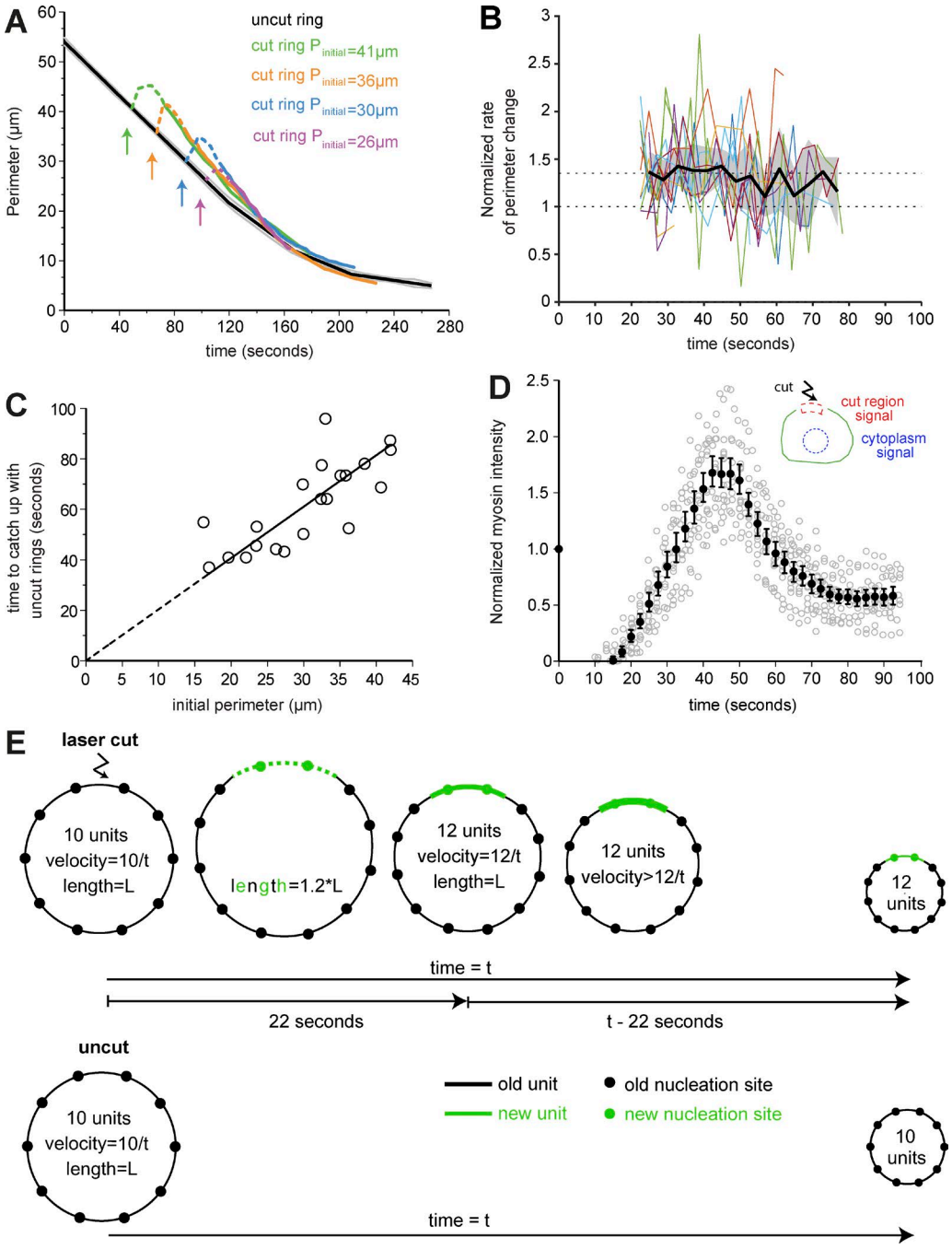

Figure 5. **Repaired rings close faster and catch up with uncut control rings.** (A) Perimeter versus time plot of four cut rings with initial perimeters of 41, 36, 30, and 26 µm. The dashed portion of colored lines corresponds to time points from 0 to ~22 s, for which part of the measured perimeter corresponds to the outline of cortical myosin$^{NMY\text{-}2}$::GFP labeling. The mean perimeter for uncut rings is in black, with gray lines indicating the 95% CI (data as in Fig. S1 C). Arrows indicate moment of laser cut. (B) Normalized ratio of perimeter change over time after cut (n = 15; see Fig. S1 F and Materials and methods for details). Colored lines represent individual examples, and the black line shows the mean. The dashed lines indicate normalized ratios of 1 and 1.35 (mean of normalized velocities >1 over the time period of 22–55 s after the laser cut). The gray area represents the 95% CI of the mean curve. (C) Time required for cut rings to catch up with the perimeter of uncut rings plotted against initial perimeter (n = 21; R^2 = 0.59 and r = 0.76; P < 0.0001). (D) Normalized myosin fluorescence intensity levels plotted against time after cut for rings with initial perimeters between 16 and 42 µm (see Fig. S3 A for method). Black dots represent mean intensities (see Materials and methods for details) with 95% CI error bars; gray circles represent individual measurements. (E) An increase in constriction velocity proportional to the gap size can be explained by the contractile unit model. When a ring is cut, the plasma membrane retracts at the site of the cut, and contractile units (green) assemble de novo at nucleation sites (green circles) distributed along the plasma membrane. This increases the total number of units in the ring and the overall velocity of constriction after gap repair relative to uncut control rings. We propose that subsequent myosin hyperaccumulation (thick green line) transiently increases tension locally along the new units and promotes faster shortening of the repaired ring, leading to an overall higher constriction velocity than expected by serial incorporation of new units.

Published December 13, 2016

or cortex and sustain tension in the severed ring, which explains why a severed ring does not fall apart and exhibits only minimal change in curvature. Our measurements of arc length and gap size after laser cutting reveal that tension within the contractile ring increases during constriction, concomitantly with a decrease in net cortical tension at the ingression site. Furthermore, we show that the increase in ring tension occurs even when cortical tension is substantially reduced and myosin activity is partially compromised. Our mechanical analysis suggests that in the early phases of constriction, the ring primarily resists cortical or membrane tension but works increasingly against other forces, which we suggest is caused by increased surface area behind the ring as it gets smaller. Therefore, contributions of additional force components should be considered in future models of ring constriction.

We show that at any time during constriction, gaps varying in size up to fourfold are efficiently repaired with identical kinetics in an actin filament polymerization–dependent manner, and that multiple sites of myosin recruitment are present during the repair of larger gaps. We speculate that those discrete recruitment sites correspond to nucleation foci on the "naked" plasma membrane exposed after a laser cut, from which new actin filaments are polymerized and contractile units are assembled. Such nucleation sites may correspond to points where contractile units are anchored to the plasma membrane, allowing for tension transmission between neighboring units and for lateral tension transmission to the membrane and remaining cortex.

The rapid kinetics of gap repair highlights the remarkable capacity for local remodeling of contractile ring structure throughout constriction, which makes cytokinesis a highly robust process unlikely to fail once the contractile ring has assembled. Importantly, the contractile units assembled de novo at the site of the gap increase the total number of units in the repaired ring. As the overall velocity of ring constriction is proportional to the total number of units, the incorporation of additional units into repaired rings provides an explanation for a proportional increase in constriction velocity (Fig. 5 E). In addition, it is conceivable that local hyperaccumulation of myosin reflects parallel incorporation, increasing the cross-sectional force capacity in the newly assembled units. Myosin hyperaccumulation would increase ring tension transiently and thereby work against resistive mechanical components, such as viscous drag and surface tension, in a dynamic force balance at a faster shortening velocity. Thus, the acceleration of repaired rings may be promoted by both the gain of additional contractile units and transient increase of local myosin density at the site of the laser cut. However, we note that in some cases, myosin levels drop to stabilization levels before ring slowdown (Fig. S3, D–F). This argues against higher myosin density and higher force capacity as the sole cause for increased constriction velocity.

The reason why myosin hyperaccumulates in the repair region remains unclear. Interestingly, a transient local overshoot of myosin was also reported after bleb retraction in metaphase cells (Biro et al., 2013). We hypothesize that, in analogy to what occurs after bleb retraction, the local spike of myosin in the contractile ring is triggered by local deformation of the plasma membrane at the cut site. Finally, our analyses fit with previous demonstrations of limited ring edge recoil and repair of contractile rings bordering plasma membrane wounds in *Xenopus* oocytes (Mandato and Bement, 2001). It would be interesting to assess whether local actomyosin hyperaccumulation and ring acceleration are also observed in this context, as these responses may be universal features of actomyosin contractile rings.

Materials and methods

C. elegans strains

Strains used in this study are listed in Table S1 and were maintained at 20°C.

Live imaging

Live imaging of one- or four-cell *C. elegans* embryos was performed under no compression at 23°C. Adult hermaphrodites were dissected in M9 buffer (86 mM NaCl, 42 mM Na_2HPO_4, 22 mM KH_2PO_4, and 1 mM $MgSO_4.7H_2O$), and embryos were placed in the wells of imaging chambers as shown in Fig. 4 B (Carvalho et al., 2011). In the experiments with latrunculin A (Sigma-Aldrich) or propidium iodide, adult hermaphrodites were dissected in meiosis medium (25 mM Hepes, pH 7.4, 5 mg/ml insulin, 20% heat-inactivated FBS, and 60% Leibowitz-15 medium; see Acute drug treatment method section for details). Images were acquired with a spinning-disk confocal system with a CSU-X1 confocal spinning-disk head (Yokogawa Electric Corporation) mounted on an inverted microscope (TE2000U; Nikon) equipped with an electron-multiplying charge-coupled device camera (iXon 897+; Andor Technology), a 100× 1.4 NA oil-immersion Plan-Apochromat objective (Nikon), and 488-nm and 561-nm lasers (Coherent). Laser shuttering and microscope hardware were controlled using NIS-Elements software (Nikon) and a digital-to-analogue converter card (PCI 8733; National Instruments).

Laser microsurgery

Laser microsurgery in constricting contractile rings was performed by using the imaging objective (1.4 NA) to focus the second harmonic beam (532-nm wavelength) of a pulsed Nd:YAG laser (FQ-500-532; Elforlight), which was injected into the microscope stand through a secondary filter turret (stage-up kit). Pulse width was 10 ns, and pulse energy was 1.5–2 µJ, with the sample being exposed to a 1-kHz pulse train for 800 ms. The laser spot at the sample was ∼0.5 µm wide in the x–y plane and at least ∼0.5 µm wide along the optical axis. The scale of the ablation volume is comparable but larger than the laser spot volume, which is a result of the requirement that the laser intensity surpass the ablation threshold intensity across the full contractile ring width. Laser microsurgery was performed at different stages of ring constriction at ring perimeters between 11 µm and 49 µm. Image acquisition was initiated before the ring reached the desired stage of constriction. By that time, the embryo was moved to have the ring positioned in the laser microsurgery target site, and the laser cut was performed. It took on average 1.6 s for the laser cut procedure, during which image acquisition was paused. For the experiments in Fig. 1 (C–E), two or more sequential cuts were made in the same constricting ring, either in the same region, with the second cut being inflicted where the repair from the first cut occurred (Fig. 1 C), or in neighboring regions along the ring (Fig. 1 D). To obtain cuts in neighboring regions, the cuts were inflicted ∼20 s apart. In this case, image acquisition was stopped before the first cut and only resumed after the second cut. To keep the ring continuously open, 22 consecutive cuts were performed in the same region of the ring (Fig. 1 E).

To monitor contractile ring behavior immediately after laser microsurgery, a single image was acquired in the 488-nm channel every second; to follow the repair and constriction after laser microsurgery, 5 × 0.5–µm, 7 × 0.5–µm, or 7 × 1.0–µm z stacks were collected in the 488-nm channel every 1.7 s, 2.32 s, or 3.2 s, respectively (fastest acquisition mode). To monitor contractile ring constriction of uncut rings, 7 × 0.5–µm or 11 × 1.0–µm z stacks were collected every 2.32 s or 10 s, respectively.

Published December 13, 2016

Plasma membrane behavior after laser cutting was monitored in four-cell embryos expressing a plasma membrane probe (pleckstrin homology [PH] domain PLC-1 Δ1) fused with GFP (PH::GFP; Audhya et al., 2005) and myosin$^{NMY\text{-}2}$::mCherry. The mCherry signal enabled ring visualization until the laser cut was performed. After the cut, the mCherry signal was photobleached, and the behavior of the membrane probe in the 488-nm channel was followed by collecting a 5 × 1.0–µm z stack every 4.3 s (Fig. S2 F).

When testing for plasma membrane wounding (Fig. S2, B and C), cortical imaging of permeable (perm-1 partially depleted, see Acute drug treatment method section) or impermeable one-cell embryos expressing myosin$^{NMY\text{-}2}$::GFP or PH::GFP was performed by acquiring seven z planes, 0.5 µm apart on the cortex of the embryo closer to the coverslip, every 2.32 s. Laser microsurgery was executed after anaphase onset and before contractile ring ingression with the conditions used to cut rings described at the beginning of this section. In these experiments, embryos were placed in meiosis medium with or without 5 µg/µl propidium iodide to assess influx after laser cutting. A plane through the center of the embryo was acquired at the end of the experiment to assess cytokinesis completion.

Image analysis, quantifications, and statistics

All measurements and image processing were done using Fiji (ImageJ; National Institutes of Health; Schindelin et al., 2012; Schneider et al., 2012). Z stacks were projected using the maximum intensity projection tool (Figs. 1; 3 F; 4, C and D; S1 A; and S2). Images within each panel were scaled equally. Kymographs shown in Figs. 1 (B–D), 2 (A and H), and 3 A were obtained using the 3D project tool. A region in maximum intensity projections or single sections that included the area of the laser cut were selected to create the kymographs (Fig. S1 F). 3D rotations of cut-constricting rings in Fig. S2 A were generated using the 3D volume view tool in NIS-Elements. Linear regressions and statistical analyses were performed with Prism 6.0 (GraphPad Software). R^2 denotes the coefficient of determination of the linear regression; r denotes Pearson's correlation coefficient. All error bars represent the 95% CI of the mean. Velocity calculations were done using Matlab (MathWorks Inc.).

Measurement of contractile ring perimeter and mean constriction velocity during ring constriction. All measurements were performed on constricting rings of ABa or ABp cells expressing myosin$^{NMY\text{-}2}$::GFP, with the exception of some of the measurements presented in Fig. S3 B, which were done in cells expressing lifeAct::GFP. For uncut rings, the ABa and ABp ring perimeter was determined by manually tracing the ring outline in maximum intensity projections of z stacks using the segmented line tool in Fiji and reading the length of the total segmented line. Data from multiple rings were temporally aligned and averaged by calculating the arithmetic mean of ring perimeters within a time frame (Fig. S1 D). We resolved four phases of the time–perimeter curve by fitting each phase to a linear trend and obtaining correlation values (R^2) close to 1.00. The equations of the linear trends were $y = -0.27x + 46.9$, for ring perimeters between 47.1 µm and 22.8 µm; $y = -0.20x + 40.7$, for ring perimeters between 20.6 µm and 12.5 µm; $y = -0.11x + 28.0$, for ring perimeters between 11.1 µm and 7.7 µm; and $y = -0.04x + 14.6$, for ring perimeters between 7.0 µm and 5.0 µm (Figs. 5 A and S3 F). These functions were used to align the perimeter curves from cut rings to those of uncut rings.

The velocity of constriction of individual uncut rings was calculated for pairs of consecutive time points by dividing the difference in perimeter by the time interval (first order difference method; Fig. S1 E). Data from multiple rings were averaged. The mean of data points that fell in overlapping 5-µm intervals was calculated and plotted against the perimeter at the center of each interval.

For cut rings, ring perimeter was determined as described in the first paragraph for uncut rings. In the period of time from the cut until repair completion (0–22 s), a portion of the measured perimeter corresponded to the outline of the cortex as judged by cortical myosin$^{NMY\text{-}2}$::GFP labeling (Fig. 5 A, dashed lines). Individual cut ring perimeter traces were aligned with the fit linear trends for uncut rings relative to the time point just before the cut (Figs. 5 A and S3 F).

Measurement of gap size, arc length of the severed ring, and time of gap repair. Gap size measurements were performed in single sections or in maximum-intensity z projections by manually tracing a straight line between the severed ends for each time point during the ∼10 s after laser microsurgery (Fig. 2, B and C; and Fig. S2 D). After the first 10 s, the gap started being filled with contractile ring material, and measuring its size became impossible. Gap size was normalized to the ring perimeter before the cut (initial perimeter) in Fig. S2 D. The maximum gap size was plotted against the initial perimeter in Fig. 2 D. The arc length of the open ring within the first 10 s after the cut was measured by manually tracing a line from the left severed end to the right severed end along the ring (Fig. 2 B). Ring recoil (Δl; Fig. 2 E), strain of the ring (ε; Fig. 2 F), and cortical relaxation (gap size minus Δl; Fig. 2 G) were determined after measuring arc length or gap size at the time point of 3.6 or 3.9 s after laser cutting, which was the earliest possible time point (these measurements had to be done in z projections of at least five z sections). Any significant length changes caused by shortening between ablation and the first time point thereafter (Fig. 2 J) were not considered in the calculations. Ring recoil (Δl) was approximated by subtracting the ablated length (0.5 µm) and arc length from the initial ring perimeter. The strain of the ring—the length change caused by tension divided by the length at rest (loss of tension)—was approximated by dividing Δl by the arc length. The values for Δl and ε correspond to approximations because we were not able to determine Δl immediately after laser ablation but only a few seconds later, and a small part of the ring is destroyed during ablation. The rate of change of the arc length during the first 8 s after laser cutting was determined by linear regression and plotted against initial perimeter (Fig. 2 J). The time of gap repair was defined as the interval between the time point just before the laser cut and the time point when the gap was completely filled in with myosin$^{NMY\text{-}2}$::GFP (Fig. 3 B).

Measurement of instantaneous ring constriction velocities after laser cut. The instantaneous rate of change of perimeter Δ_t p (= constriction velocity) was determined with the first order difference method for time points after completion of repair and with perimeters >19 µm (at which point rings approach the spindle midzone and slow down; Carvalho et al., 2009). The difference in perimeter between time points t[i + 1] and t[i] was divided by the interval between those time points for all frames i of a video: Δ_t p(t[i]) = (p(t[i + 1])) − p(t[i])/(t[i + 1] − t[i]). The rate of change of the perimeter for the reference uncut ring, Δ_t P(t), and for every cut ring, Δ_t p{j}(t), $j = 1…n$, was calculated. P(t) represents the mean of ABp rings. For cut rings, Δ_t p{j}(t) was normalized to Δ_t P, where P(T) = p{j}(t); i.e., the time point T for which the perimeter of the uncut ring matched the cut ring was determined by interpolation, and the velocity at this time point T was used for normalization: Ω{j}(t) = Δ_t p{j}(t)/Δ_t P(T), for all traces $j = 1…n$ (Fig. S1 G). The velocity Δ_t P(T) was determined by interpolation of T within the discrete values of Δ_t P(t[i]). A mean curve for Ω{j}(t) was calculated by temporally aligning the Ω{j} with respect to the time point for severing, overlaying all Ω{j} (Fig. 5 B), dividing the time axis in equal bins with size Δt = 4 s, and filling each bin with the normalized velocities Ω{j}(k • Δt < t < (k + 1) • Δt), $k = 1…M$, with M equaling the number of bins. Then, the arithmetic mean of the values in each bin was calculated. Similarly, the SEM = SD/sqrt(N[k]), with N[k] equaling the number of values in bin k, was determined for all M bins, and the 95% CI was

Published December 13, 2016

estimated as 1.96 × SEM. The resulting data were plotted with respect to the center of the bin, $\Delta t/2 + k \bullet \Delta t$, $k = 1 \ldots M$.

The time interval for cut rings to catch up with uncut rings was defined as the interval between the time point just before the laser cut and the time point when the repaired ring reached a perimeter that was within the region of the uncut ring perimeter mean plus 95% CI (Figs. 5 C and S3 D).

Quantification of myosin fluorescence levels after laser cut. The myosin$^{NMY\text{-}2}$::GFP mean intensity level in the cut region was quantified within a box 0.7 µm thick and 2.0 µm wide drawn over the region where the cut was inflicted; the dimensions of the box were kept constant for all time points measured before and after the cut. A circular region in the cytoplasm, which decreased in size as the ring constricted, was used to quantify the mean intensity of the myosin$^{NMY\text{-}2}$::GFP cytoplasmic signal. The cytoplasmic signal was subtracted from the mean intensity in the cut region, and values were normalized to the mean myosin intensity before the cut (Figs. 5 D and S3, A and F). Individual traces revealed that myosin levels increased to a maximum level and then decreased and stabilized until the end of ring constriction (Fig. 5 D). The myosin$^{NMY\text{-}2}$::GFP level profile revealed reproducible kinetics regardless of ring perimeter before the cut. Therefore, normalized profiles from multiple cut rings were aligned to the time point before the cut and plotted against the time after the cut (Fig. 5 D). The mean of data points that fell in overlapping 5-s intervals was calculated and plotted against the time at the center of each interval. The time between the laser cut and maximum myosin accumulation is shown in Fig. S3 B. Quantification of actin levels in embryos expressing lifeAct::GFP was performed as described for myosin$^{NMY\text{-}2}$::GFP (Fig. S3 A). The time interval from the laser cut until the stabilization of myosin levels is plotted against the time it took for cut rings to catch up with uncut rings in Fig. S3 D.

To assess the correlation between increased myosin levels in the region of gap repair and the increase of ring constriction velocity, we determined the interval during which myosin levels in the repaired region were greater than the myosin stabilization level (Fig. S3, C, D, and F). The latter, which is represented by the vertical orange dashed lines in Fig. S3 C, was plotted against the time interval from completion of repair to catch up with uncut rings (Fig. S3 E). To assess the extent of overlap between increased constriction velocity and myosin hyperaccumulation, graphs of the perimeter versus time and normalized myosin intensity versus time of individual examples were overlaid, and two representative examples are shown in Fig. S3 F.

RNAi

For feeding RNAi, a 563-bp region of the mlc-4 gene (C56G7.1) was amplified with primers 5′-CAACAGATATCGCCTCCCGCAAAA CCG-3′ and 5′-CCCCCGATATCCTTAATCGGAGCATCTC-3′ and cloned into the RNAi feeding vector L4440, which was transformed into HT115 *Escherichia coli* bacteria.

The RNAi bacterial clone was grown until an OD of 1.6 in 50 ml Luria broth medium containing 12.5 µg/ml tetracycline and 50 µg/ml ampicillin overnight at 37°C. The overnight culture was centrifuged for 10 min at 2,500 *g*. Before bacterial inoculation, the RNAi plates were dried for 2 h in a 37°C incubator. Then, 100 µl of a 1:1:1 mix of 50 µg/ml ampicillin, 0.23 mg/ml IPTG, and 12.5 µg/ml tetracycline was added to the dried RNAi plates. The supernatant was removed and the cell pellet was resuspended in 2.5 ml Luria broth medium containing 12.5 µg/ml tetracycline, 50 µg/ml ampicillin, and 0.23 mg/ml IPTG. The RNAi plate was inoculated with 75 µl of bacterial culture. The expression of double-stranded RNA was induced overnight at room temperature and in the dark. 25–30 (old) L4 stage worms were transferred onto the mlc-4 (RNAi) plate and incubated at 20°C for 24–28 h before dissection for imaging.

Acute drug treatment

Acute drug treatments were performed in permeabilized *C. elegans* embryos as previously described (Carvalho et al., 2011). To obtain permeabilized embryos, perm-1 RNAi conditions were optimized as suggested by Carvalho et al. (2011). In brief, 25–30 (old) L4 worms were placed on a plate containing 0.005 mM IPTG and HT115 (DE3) bacteria expressing double-stranded RNA against perm-1 and were left at 20°C for 14–18 h. Embryos were placed in meiosis medium (see the Laser microsurgery section for the recipe), and 0.5 µM latrunculin A was added after the initiation of constriction.

Myosin distribution around ring circumference

Myosin distribution along the ring in Fig. 3 E was analyzed using Mathematica (Wolfram Research) and ImageJ with custom-made plugins. The z stack sum projection was computed, and background was subtracted for each time frame t_i. A 3-pixel-wide polyline was manually traced along the ring for each time point, and the intensity profile ($A_i(x) = A(x, t_i)$) was generated. The profiles $A_i(x)$ were normalized to the maximal value of the first profile ($A_1 = \max\{A_1(x)\}$) and smoothed using the exponential moving average with the smoothing constant 0.2. The sequence of the normalized smoothed profiles ($A^s_i(x) = A_i(x)/A_1$) corresponds to a surface which was presented as a heat map showing the levels A^s = constant. The length of each profile d_i corresponds to the ring perimeter, and the time-ordered sequence of d_i produces the perimeter dynamics.

Online supplemental material

Fig. S1 shows details about contractile ring constriction in the four-cell *C. elegans* embryo. Fig. S2 shows that our laser microsurgery experiments do not cause plasma membrane damaging and shows gap behavior in embryos expressing fluorescent probes for the contractile ring and plasma membrane. Fig. S3 shows characterization details of the myosin hyperaccumulation in the repaired region. Video 1 shows two contractile rings snapping open, getting repaired, and completing constriction in the same time as uncut rings after laser microsurgery. Video 2 (Fig. 1 C) shows the contractile ring's ability to repair itself after two sequential cuts in the same region. Video 3 (Fig. 1 E) shows that a contractile ring that has been kept continuously open is able to keep constricting. Video 4 (Fig. 3 F) shows the new nucleation sites from which the gap seems to be filled in a cut ring in which the first attempt at gap repair failed but second succeeded. Table S1 contains a list of the worm strains used in this study.

Acknowledgments

We thank Francisco Calheiros for critical reading of the manuscript and Alex Mogilner for helpful discussions.

This project has received funding from the European Research Council (grants 640553, 260892, and 338410), Fundo Europeu de Desenvolvimento Regional (FEDER) funds through the Operational Competitiveness Program (COMPETE), national funds through Fundação para a Ciência e a Tecnologia (FCT) under the project FCOMP-01-0124-FEDER-028255 (PTDC/BEX-BCM/0654/2012), Fundação Luso-Americana para o Desenvolvimento Life Science 2020, and the Louis-Jeantet Young Investigator Award to H. Maiato. A.X. Carvalho, R. Gassmann, and I.A. Telley have FCT Investigator positions funded by FCT and cofunded by the European Social Fund through Programa Operacional Temático Potencial Type 4.2 promotion of scientific employment. A.M. Silva holds an FCT fellowship (SFRH/BPD/95707/2013). D.S. Osório was cofunded by the Programa Operacional Regional do Norte under the Quadro de

Referência Estratégico Nacional through FEDER and by FCT grant NORTE-07-0124-FEDER-000003 (Cell Homeostasis Tissue Organization and Organism Biology).

The authors declare no competing financial interests.

Submitted: 20 May 2016
Revised: 14 September 2016
Accepted: 2 November 2016

References

Audhya, A., F. Hyndman, I.X. McLeod, A.S. Maddox, J.R. Yates III, A. Desai, and K. Oegema. 2005. A complex containing the Sm protein CAR-1 and the RNA helicase CGH-1 is required for embryonic cytokinesis in *Caenorhabditis elegans*. *J. Cell Biol.* 171:267–279. http://dx.doi.org/10.1083/jcb.200506124

Bement, W.M., and D.G. Capco. 1991. Analysis of inducible contractile rings suggests a role for protein kinase C in embryonic cytokinesis and wound healing. *Cell Motil. Cytoskeleton.* 20:145–157. http://dx.doi.org/10.1002/cm.970200207

Biro, M., Y. Romeo, S. Kroschwald, M. Bovellan, A. Boden, J. Tcherkezian, P.P. Roux, G. Charras, and E.K. Paluch. 2013. Cell cortex composition and homeostasis resolved by integrating proteomics and quantitative imaging. *Cytoskeleton (Hoboken).* 70:741–754. http://dx.doi.org/10.1002/cm.21142

Carvalho, A., A. Desai, and K. Oegema. 2009. Structural memory in the contractile ring makes the duration of cytokinesis independent of cell size. *Cell.* 137:926–937. http://dx.doi.org/10.1016/j.cell.2009.03.021

Carvalho, A., S.K. Olson, E. Gutierrez, K. Zhang, L.B. Noble, E. Zanin, A. Desai, A. Groisman, and K. Oegema. 2011. Acute drug treatment in the early *C. elegans* embryo. *PLoS One.* 6. http://dx.doi.org/10.1371/journal.pone.0024656

Collinet, C., M. Rauzi, P.-F. Lenne, and T. Lecuit. 2015. Local and tissue-scale forces drive oriented junction growth during tissue extension. *Nat. Cell Biol.* 17:1247–1258. http://dx.doi.org/10.1038/ncb3226

Colombelli, J., A. Besser, H. Kress, E.G. Reynaud, P. Girard, E. Caussinus, U. Haselmann, J.V. Small, U.S. Schwarz, and E.H.K. Stelzer. 2009. Mechanosensing in actin stress fibers revealed by a close correlation between force and protein localization. *J. Cell Sci.* 122:1665–1679. http://dx.doi.org/10.1242/jcs.042986

Founounou, N., N. Loyer, and R. Le Borgne. 2013. Septins regulate the contractility of the actomyosin ring to enable adherens junction remodeling during cytokinesis of epithelial cells. *Dev. Cell.* 24:242–255. http://dx.doi.org/10.1016/j.devcel.2013.01.008

Green, R.A., E. Paluch, and K. Oegema. 2012. Cytokinesis in animal cells. *Annu. Rev. Cell Dev. Biol.* 28:29–58. http://dx.doi.org/10.1146/annurev-cellbio-101011-155718

Guillot, C., and T. Lecuit. 2013. Adhesion disengagement uncouples intrinsic and extrinsic forces to drive cytokinesis in epithelial tissues. *Dev. Cell.* 24:227–241. http://dx.doi.org/10.1016/j.devcel.2013.01.010

Herszterg, S., A. Leibfried, F. Bosveld, C. Martin, and Y. Bellaiche. 2013. Interplay between the dividing cell and its neighbors regulates *adherens* junction formation during cytokinesis in epithelial tissue. *Dev. Cell.* 24:256–270. http://dx.doi.org/10.1016/j.devcel.2012.11.019

Kamasaki, T., M. Osumi, and I. Mabuchi. 2007. Three-dimensional arrangement of F-actin in the contractile ring of fission yeast. *J. Cell Biol.* 178:765–771. http://dx.doi.org/10.1083/jcb.200612018

Kumar, S., I.Z. Maxwell, A. Heisterkamp, T.R. Polte, T.P. Lele, M. Salanga, E. Mazur, and D.E. Ingber. 2006. Viscoelastic retraction of single living stress fibers and its impact on cell shape, cytoskeletal organization, and extracellular matrix mechanics. *Biophys. J.* 90:3762–3773. http://dx.doi.org/10.1529/biophysj.105.071506

Mabuchi, II, S. Tsukita, S. Tsukita, and T. Sawai. 1988. Cleavage furrow isolated from newt eggs: contraction, organization of the actin filaments, and protein components of the furrow. *Proc Natl Acad Sci USA.* 85:5966–5970.

Mandato, C.A., and W.M. Bement. 2001. Contraction and polymerization cooperate to assemble and close actomyosin rings around *Xenopus* oocyte wounds. *J. Cell Biol.* 154:785–797. http://dx.doi.org/10.1083/jcb.200103105

Munjal, A., J.-M. Philippe, E. Munro, and T. Lecuit. 2015. A self-organized biomechanical network drives shape changes during tissue morphogenesis. *Nature.* 524:351–355. http://dx.doi.org/10.1038/nature14603

Sain, A., M.M. Inamdar, and F. Jülicher. 2015. Dynamic force balances and cell shape changes during cytokinesis. *Phys. Rev. Lett.* 114:048102. http://dx.doi.org/10.1103/PhysRevLett.114.048102

Savoian, M.S., A. Khodjakov, and C.L. Rieder. 1999. Unilateral and wandering furrows during mitosis in vertebrates: implications for the mechanism of cytokinesis. *Cell Biol. Int.* 23:805–812. http://dx.doi.org/10.1006/cbir.1999.0477

Schindelin, J., I. Arganda-Carreras, E. Frise, V. Kaynig, M. Longair, T. Pietzsch, S. Preibisch, C. Rueden, S. Saalfeld, B. Schmid, et al. 2012. Fiji: an open-source platform for biological-image analysis. *Nat. Methods.* 9:676–682. http://dx.doi.org/10.1038/nmeth.2019

Schneider, C.A., W.S. Rasband, and K.W. Eliceiri. 2012. NIH Image to ImageJ: 25 years of image analysis. *Nat. Methods.* 9:671–675. http://dx.doi.org/10.1038/nmeth.2089

Stachowiak, M.R., C. Laplante, H.F. Chin, B. Guirao, E. Karatekin, T.D. Pollard, and B. O'Shaughnessy. 2014. Mechanism of cytokinetic contractile ring constriction in fission yeast. *Dev. Cell.* 29:547–561. http://dx.doi.org/10.1016/j.devcel.2014.04.021

Tinevez, J.-Y., U. Schulze, G. Salbreux, J. Roensch, J.-F. Joanny, and E. Paluch. 2009. Role of cortical tension in bleb growth. *Proc. Natl. Acad. Sci. USA.* 106:18581–18586. http://dx.doi.org/10.1073/pnas.0903353106

Turlier, H., B. Audoly, J. Prost, and J.-F. Joanny. 2014. Furrow constriction in animal cell cytokinesis. *Biophys. J.* 106:114–123. http://dx.doi.org/10.1016/j.bpj.2013.11.014

Vicente-Manzanares, M., X. Ma, R.S. Adelstein, and A.R. Horwitz. 2009. Non-muscle myosin II takes centre stage in cell adhesion and migration. *Nat. Rev. Mol. Cell Biol.* 10:778–790. http://dx.doi.org/10.1038/nrm2786

Zhang, W., and D.N. Robinson. 2005. Balance of actively generated contractile and resistive forces controls cytokinesis dynamics. *Proc. Natl. Acad. Sci. USA.* 102:7186–7191. http://dx.doi.org/10.1073/pnas.0502545102

Silva et al., https://doi.org/10.1083/jcb.201605080

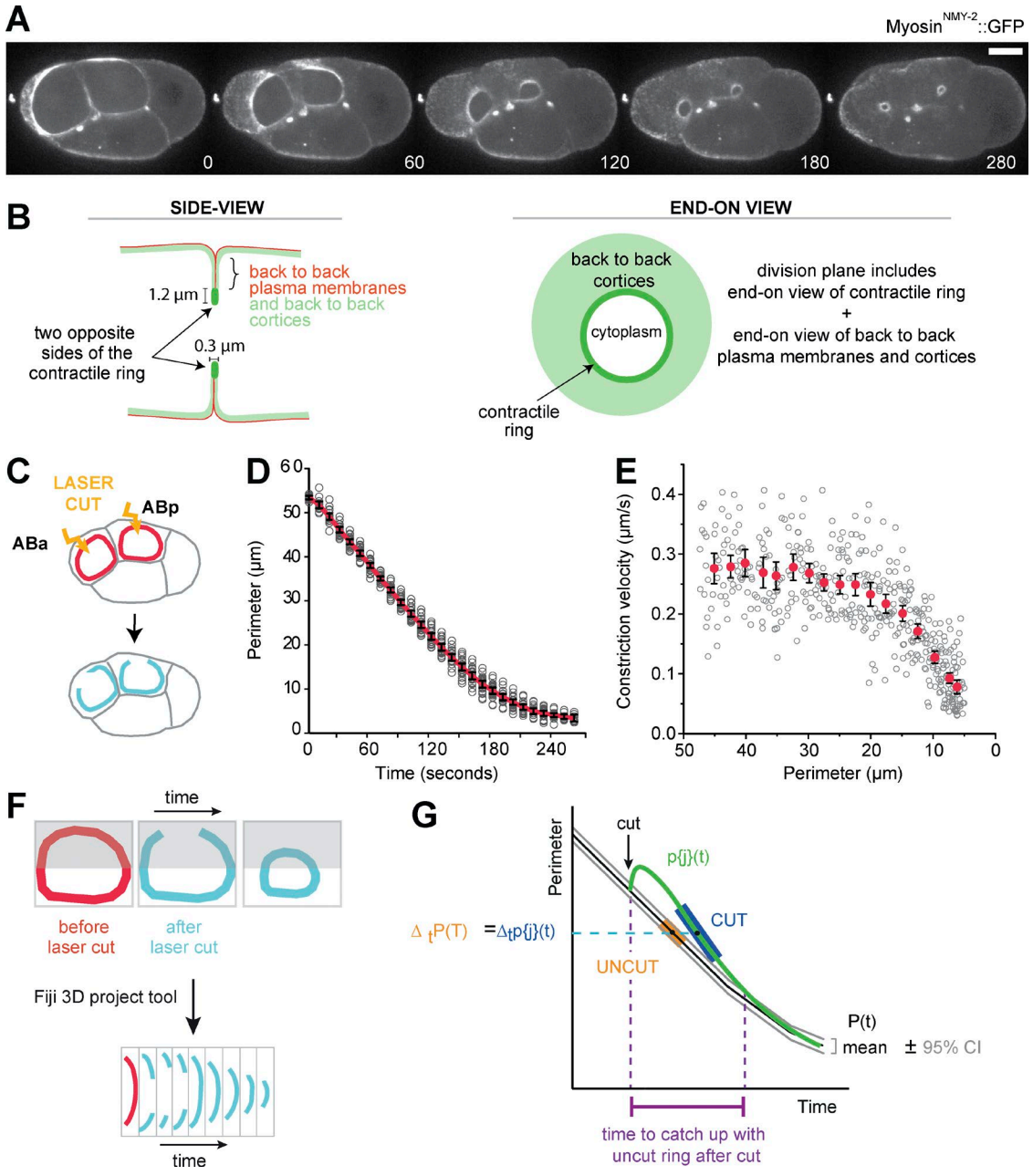

Figure S1. **End-on view time-lapse imaging of the contractile ring of AB cells in the four-cell *C. elegans* embryo.** (A) End-on view of constricting contractile rings in a four-cell *C. elegans* embryo expressing myosin^{NMY-2}::GFP. The ABa and ABp cells undergo ring constriction parallel to the imaging plane. Time is in seconds. Bar, 10 µm. (B) Schematic illustrating that the contractile ring sits at the tip of a septum. (C) Schematic of a four-cell embryo illustrating where laser cuts were inflicted. The contractile ring in the early *C. elegans* embryo is estimated to be 1.2 µm wide and 0.3 µm thick (Carvalho et al., 2009). (D) Perimeter versus time plot for contractile ring constriction in ABa and ABp cells (n = 22). The red line represents the mean perimeter with black error bars denoting the 95% CI of the mean. Gray circles show individual values. (E) Mean constriction rate (red dots with error bars representing a 95% CI; see Materials and methods for details) plotted against the decreasing ring perimeter in ABa and ABp cells (n = 22). Gray circles show individual values. (F) Schematic illustrating how kymographs of the cut region were generated for Fig. 1 (B–D), Fig. 2 (A and H), and Fig. 3 A. (G) Schematic illustrating how instantaneous rates of perimeter change in Fig. 5 B were calculated.

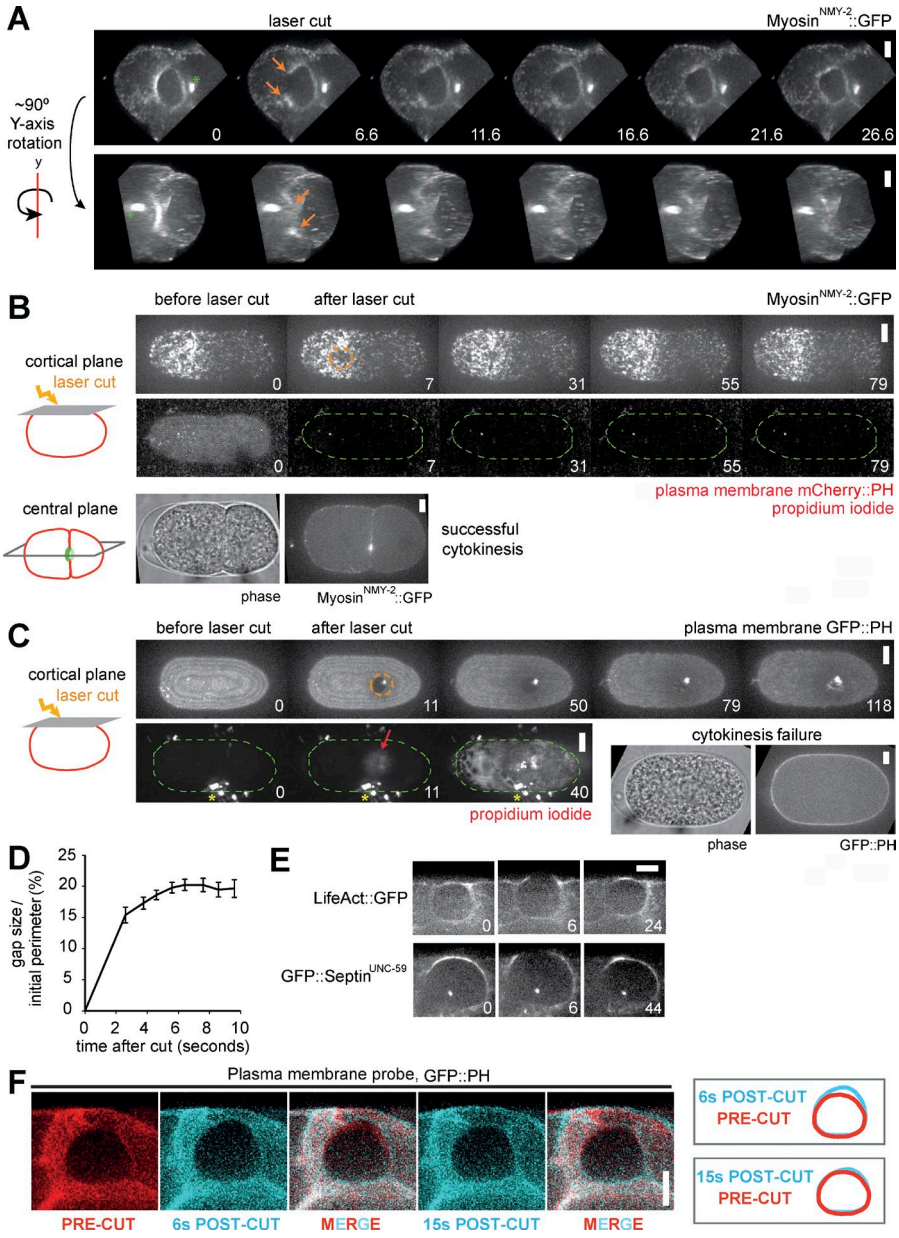

Figure S2. **Characterization of gap formation and gap repair in embryos expressing fluorescent probes for the contractile ring and plasma membrane.** (A) 3D volume of a laser-cut ABa ring expressing myosin^{NMY-2}::GFP before (top row) and after (bottom row) rotation of unprojected z stacks by ~90° around the y axis. Orange arrows point to the two severed ends of the contractile ring after laser microsurgery. The green asterisk indicates the position of a midbody from a previous division as reference point. (B) In our laser microsurgery experiments, the contractile ring was cut without generating a hole in the plasma membrane. Permeabilized one-cell embryos expressing myosin^{NMY-2}::GFP were placed in medium with propidium iodide to check for influx after laser microsurgery. The same laser ablation conditions used to cut the contractile ring were used to hit the cortical myosin layer end-on during early cytokinesis. A circular region devoid of myosin^{NMY-2}::GFP was immediately observed (orange dashed circle, top row of stills) and was refilled with myosin^{NMY-2}::GFP signal in ~70 s without forming a distinct myosin ring (cortical plane, top row). Propidium iodide did not enter the embryo (green dashed outlines correspond to the boundary of the embryo, and no propidium iodide is observed within the outlined region in the second row of stills). The embryo kept undergoing cell division (two-cell embryo at the bottom in phase and myosin^{NMY-2}::GFP images). Note that the signal in the first still of the second row is a result of the probe PH::mCherry, a PH domain fused to mCherry, which marks the plasma membrane and is also expressed in these embryos. The PH::mCherry signal is photobleached by laser microsurgery. (C) As in B, but in permeabilized one-cell embryos expressing a fluorescent probe for the plasma membrane, PH::GFP. Invariably, a circular region devoid of GFP was immediately observed (orange dashed circle, top row of stills), a bright GFP spot appeared, and membrane patching of the affected area started occurring ~80 s after laser ablation. Propidium iodide entered the embryo (signal observed within the regions outlined in green in the second row of stills). The red arrow indicates the region where the propidium iodide entered the embryo, and yellow asterisks indicate debris in the imaging chamber. The embryo did not continue to divide. It is of note that when permeabilized four-cell embryos are placed in medium with propidium iodide, rings snap open (Fig. 1, A and B; and Fig. 2 A), propidium iodide does not enter the embryos, and embryos keep dividing. (D) Gap size normalized to the initial perimeter during the first 10 s after the laser cut. Data for all examples presented in Fig. 2 C are shown (n = 24). Error bars represent the 95% CI. (E) Time-lapse stills of laser microsurgery experiments performed in embryos expressing fluorescent probes for actin (lifeAct::GFP), and one of the two septins (GFP::UNC-59). (A, B, C, and E) Numbers on stills correspond to time in seconds, and time 0 corresponds to the frame before the laser cut. (F) Stills of a constricting ring cut by laser microsurgery in an embryo expressing PH::GFP to mark the plasma membrane. The overlays at the right compare the ring outlines before the cut against the ring outline 6 s after the cut (local deformation of plasma membrane) and 15 s after the cut (plasma membrane deformation no longer evident). Bars, 5 µm.

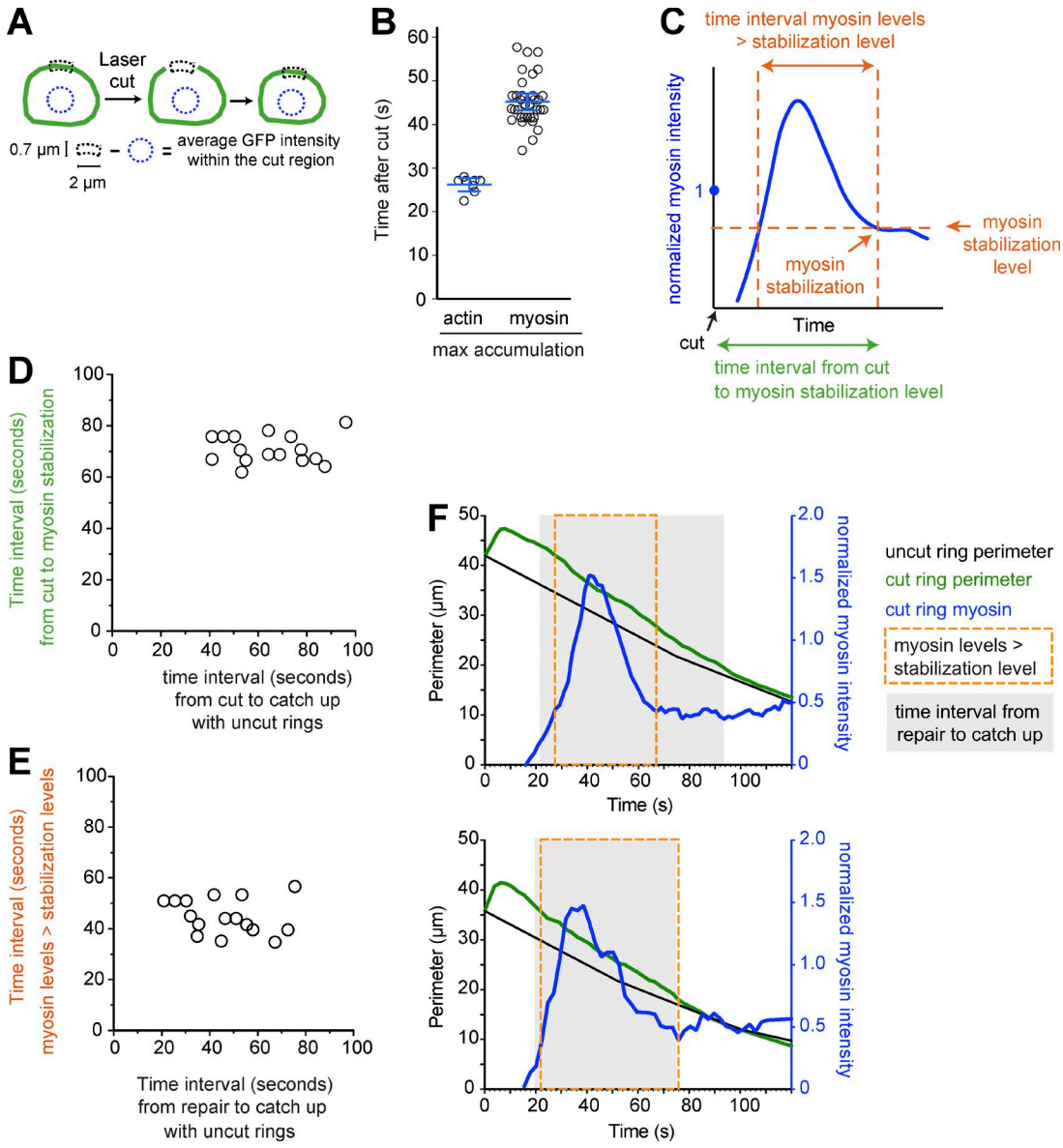

Figure S3. **Characterization of myosin hyperaccumulation after gap repair.** (A) Schematic illustrating the quantification method for mean myosin intensity levels in the cut region. A region of constant dimensions was placed over the severing region at time points just before and after the cut. Cytoplasmic signal was subtracted, and values were normalized to the mean myosin intensity before the cut. (B) Time period between laser cut and maximum accumulation of actin (lifeAct::GFP) or myosin (NMY-2::GFP) in the repaired region. Error bars represent the 95% CI of the mean. (C) Schematic illustrating how time intervals plotted in D–F were determined. (D) Time interval between laser cut and stabilization of myosin levels versus the time until cut rings caught up with the perimeters of uncut rings. (E) Time interval during which myosin levels were greater than the stabilization level versus time interval between the completion of repair and catching up. (D and E) $n = 16$; Pearson correlation test not significant. (F) Two representative examples of perimeter (green) and normalized myosin levels (blue) versus time in cut rings. The mean perimeter of uncut rings is shown in black. Normalized myosin levels in uncut rings, which remain constant throughout constriction, are not depicted. The gray area marks the time interval between completion of repair and catching up. The orange box marks the time during which myosin levels are greater than the stabilization level, as depicted in C. The top graph shows an example of a cut ring in which myosin levels stabilize before the ring perimeter catches up with that of uncut rings. The bottom graph shows an example in which myosin levels drop coincidentally with the ring perimeter catching up with that of uncut rings.

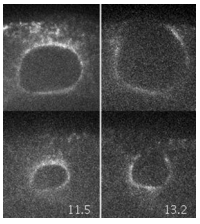

Video 1. **Contractile rings snap open, repair, and complete constriction in the same time as uncut rings after laser microsurgery.** Confocal time-lapse video of two uncut (left, top and bottom) and two laser-cut (right, top and bottom) contractile rings of the ABp cell in the four-cell embryo expressing myosin$^{NMY\text{-}2}$::GFP. Contractile rings are cut 4.6 s after the video starts, when ring perimeters are 30 µm (top right) and 16 µm (bottom right). Images are maximum intensity projections of 7.0 × 0.5–µm z stacks acquired every 2.32 s. The video playback rate is four frames per second.

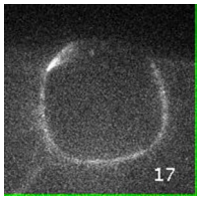

Video 2. **Contractile rings are able to repair two sequential cuts in the same region.** See Fig. 1 C. Confocal time-lapse video of a sequentially laser-cut contractile ring of the ABp cell in the four-cell stage embryo expressing myosin$^{NMY\text{-}2}$::GFP. The first cut is made 10 s after the video starts, when the ring perimeter is 38 µm. The second cut is made 44 s after the video starts, at the site where the repair from the first cut occurred, when ring perimeter is 32.5 µm. Images are single planes. Time is in seconds. The video playback rate is eight frames per second.

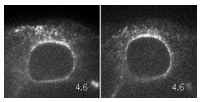

Video 3. **A continuously open ring is able to constrict.** See Fig. 1 E. Confocal time-lapse video of an uncut (left) and a laser-cut (right) contractile ring of the ABp cell in the four-cell stage embryo expressing myosin$^{NMY\text{-}2}$::GFP. The contractile ring is cut for the first time 9.4 s after the video starts, when the ring perimeter is 30.2 µm. Repair of the gap was prevented by cutting the ring continuously at the same site. The images are maximum intensity projections of 7.0 × 0.5–µm z stacks acquired every 2.32 s. Time is in seconds. The video playback rate is four frames per second.

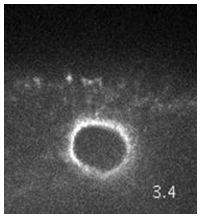

Video 4. **Multiple myosin recruitment sites are observed along the plasma membrane in large gaps.** See Fig. 3 F. Confocal time-lapse video of a laser-cut contractile ring of the ABp cell expressing myosin$^{NMY\text{-}2}$::GFP. The contractile ring is cut 6.8 s after the video starts, when ring perimeter is 14.3 µm. 22 s after the cut, the first attempt at gap repair fails, the two severed ends separate further, and a new half ring forms. Yellow arrowheads point at new myosin recruitment sites along the gap (32.2 s). The images are maximum intensity projections of 5.0 × 0.5–µm z stacks acquired every 1.67 s. Time is in seconds. The video playback rate is four frames per second.

Table S1. **List of worm strains used in this study.**

Strain	Genotype
N2	Ancestral
OD822	unc-119(ed3)III; ltSi201[pAC65; Pnmy-2::GFP; cb-unc-119(+)]II
GCP21[a]	ltIs157 [pAC16;pie-1/Life-Act::GFP; unc-119 (+)]; ltIs37 [pAA64; pie-1/mCherry::his-58; unc-119 (+)] IV
GCP57	unc-119(ed3)III; prtSi2[pAC71; Pnmy-2:nmy-2 re-encoded::mCherry::StrepTagII::3′UTRnmy-2; cb-unc-119(+)]II + unc-119(ed3) III; ltIs44 [pAA173; pie-1/GFP::PH(PLC1delta1); unc-119 (+)]
OD121	unc-119(ed3) III; ltIs20[pASM10; pie-1/GFP::unc-59; unc-119(+)]; ltIs37 [pAA64; pie-1/mCherry::his-58; unc-119 (+)] IV
GCP7	unc-119(ed3) III; ltIs44 [pAA173; pie-1/mCherry::PH(PLC1delta1); unc-119 (+)]; ltSi201[pAC65; Pnmy-2::GFP; unc-119(+)](II)

[a]*C. elegans* embryos expressing lifeAct::GFP divide with the same kinetics as those labeled with other contractile ring markers, indicating that the actin–cytoskeleton dynamics are not affected in this strain.

Reference

Carvalho, A., A. Desai, and K. Oegema. 2009. Structural memory in the contractile ring makes the duration of cytokinesis independent of cell size. *Cell.* 137:926–937. http://dx.doi.org/10.1016/j.cell.2009.03.021